

# We are IntechOpen, the world's leading publisher of Open Access books Built by scientists, for scientists

6,900

Open access books available

186,000

International authors and editors

200M

Downloads

Our authors are among the

154

Countries delivered to

TOP 1%

most cited scientists

12.2%

Contributors from top 500 universities



WEB OF SCIENCE™

Selection of our books indexed in the Book Citation Index  
in Web of Science™ Core Collection (BKCI)

Interested in publishing with us?  
Contact [book.department@intechopen.com](mailto:book.department@intechopen.com)

Numbers displayed above are based on latest data collected.  
For more information visit [www.intechopen.com](http://www.intechopen.com)



---

# Photoexcitations and Emission Processes in Organometal Trihalide Perovskites

---

Michele Cadelano, Michele Saba, Nicola Sestu, Valerio Sarritzu, Daniela Marongiu, Feipeng Chen, Roberto Piras, Francesco Quochi, Andrea Mura and Giovanni Bongiovanni

Additional information is available at the end of the chapter

<http://dx.doi.org/10.5772/61282>

---

## Abstract

Organometal halide perovskites have recently attracted widespread attention among scientists, as they combine the advantages of low-cost processability with strong light absorption, band-gap tunability from the near-infrared to the visible region of the electromagnetic spectrum, efficient light emission and charge transport. Such combination of features is unique among solution-processed materials and makes perovskites appealing for several optoelectronic applications, in particular those related to energy sustainability, which could help the advent of a new generation of low-cost but efficient solar cells and large-area light-emitting devices. This chapter reports a critical review of the efforts that scientists have made until now to understand the photophysics of organometal halide perovskites. We address the ongoing debate on the nature of the photoexcited species, namely the role played by free carriers and excitons, the determination of the exciton binding energy as a measure of the Coulomb interaction strength in these materials, the competition between radiative and non-radiative processes, the role and density of charge carrier traps, and last but not least a critical analysis of those phenomena at the base of laser action, highlighting the most relevant results and possible solutions to issues that still remain open.

**Keywords:** Hybrid perovskites, excitons, free carriers, amplified spontaneous emission, laser

---

## 1. Introduction

Organometal halide perovskites are solution-processed semiconductors showing efficient charge transport, favorable emission properties, strong light absorption and optical gap

---

tunability from the visible to the near-infrared spectrum [1–16]. Such interesting properties make these materials very appealing for the realization of solar cells and optical emitters [17–19]. Despite the widespread research activities on these novel semiconductors, some fundamental aspects of the photophysics underlying perovskites have been elusive, especially for what concerns the excited state dynamics [20–29]. For instance, due to the hybrid organic–inorganic nature of organometal perovskites, in principle it is not clear if the excited state properties are dominated by bound or unbound electron-hole states, that is excitons or free carriers. While initial reports assumed the presence of excitons, much like in organic materials, recent optical spectroscopy evidences have emerged that the majority of band-edge optical excitations at room temperature appears to be free carriers [6,22,30].

The architecture of a solar cell depends on this feature. Indeed, if the majority of photoexcited carriers happens to be bound electron-hole states, a heterojunction is necessary to split charges and then produce a current flow in a photovoltaic device. On the other hand, if photoexcitation results in the formation of free carriers, the solar cell structure is simplified, since charges are already separated and can be easily collected at the electrodes.

A lively debate has then started to understand the physical reasons that underpin the prevalence of free carriers over excitons. Clearly, within such debate, a precise and reliable determination of the exciton binding energy is of paramount importance. Reports of exciton binding energies have varied widely, from less than 5 meV to over 50 meV [22,30–37]; it has even been suggested that the exciton binding energy may be temperature-dependent, due to ionic screening effects [33,34,38].

Beyond the potential application in photovoltaics, organometal halide perovskites exhibit also excellent emission properties. In fact, amplified spontaneous emission (ASE) was also demonstrated for photoexcited carrier densities above a threshold value [17–19], representing the first step towards a laser device. Until now, many experiments probed optical amplification under impulsive excitation, meaning that the pumping pulse duration is much shorter than the typical lifetime of the excited states of the crystals [17–19,39–41]. In these kinds of experiments, ASE occurs within a sub-nanosecond time window, which is far from the continuous wave (cw) operation of a real laser device. Hence, it is not clear how long these materials can sustain optical amplification and what warming issues and parasitic processes are involved. Understanding these features is crucial in the perspective of the realization of a perovskite-based cw laser [19].

The aim of this chapter is to summarize the progress made in understanding the physics of excitons and free carriers in perovskites, both in the low excitation regime relevant for solar cells and in the high excitation regime needed for optical amplification. Experimental results obtained from optical spectroscopy measurements carried out in the Department of Physics of the University of Cagliari will be analyzed and critically compared with results published by other research groups.

Sections 2–5 of this chapter describe the absorption and the emission properties of pure and mixed methylammonium lead iodide perovskite films ( $\text{MAPbI}_3$  and  $\text{MAPbI}_{3-x}\text{Cl}_x$ , respectively), showing that the prevailing excited species in these materials is a correlated electron-hole

plasma at room temperature, from injected carrier densities typical of solar illumination to those typical to obtain light amplification [30].

An investigation about amplified spontaneous emission in organolead halide perovskites is provided in Sections 6–10, where both the temporal and the spectral photoluminescence (PL) signals have been studied under short- and long-pulsed excitation at high laser fluence, focusing on the physical parameters that allow or inhibit optical amplification in methylammonium lead iodide and bromide (MAPbBr<sub>3</sub>) perovskite thin films.

## 2. Exciton binding energy in perovskite films

A large absorption coefficient across the visible spectrum and the consequent efficient solar light harvesting is one of the strong points of perovskites. Initial works rationalized the strong absorption close to the energy-gap and the nature of optical excitations close to the band-gap in terms of excitons, as in organic semiconductors; further investigations have recently converged to state that photoexcitation results in the generation of free carriers in a wide range of pumping intensities, even at ones comparable to solar illumination, as typical of inorganic semiconductors. Such finding is consistent with small values of the exciton binding energy, for which thermal energy is sufficient to ionize excitons in free electrons and holes.

A reliable framework usually adopted in solid state physics to estimate the exciton binding energy is Elliot's theory of Wannier excitons [42], which is valid for bulk semiconductors having exciton binding energies much smaller than the energy gap (Wannier excitons). Such theory accurately describes the optical transitions near the band-gap in inorganic semiconductors like GaAs and GaP [43,44] and models the shape of the optical absorption coefficient  $\alpha(\hbar\omega)$  by the following equation:

$$\alpha(\hbar\omega) \propto \frac{\mu_{cv}^2}{\hbar\omega} \sum_j |\varphi_j(r=0)|^2 \delta(\hbar\omega - E_j) \propto \frac{\mu_{cv}^2}{\hbar\omega} \left[ \sum_j \frac{4\pi\sqrt{E_b^3}}{j^3} \delta(\hbar\omega - E_j^b) + \frac{2\pi\sqrt{E_b} \theta(\hbar\omega - E_g)}{1 - e^{-2\pi\sqrt{\frac{E_b}{\hbar\omega - E_g}}}} \right] \quad (1)$$

The absorption coefficient depends on the weighted density of electron-hole pair states, with the weight provided by the probability for an electron and a hole to be at the same position, that is  $|\varphi_j(r=0)|^2$ , while  $\varphi_j$  represents the wave functions of bound and unbound states.  $\mu_{cv}$  represents the transition dipole moment between conduction and valence bands, and  $\hbar\omega$  is the photon energy involved in the transition. In the third expression of Eq. (1), the first term describes the transitions to bound exciton states  $E_j^b$ , while the second term takes into account the band-to-band transitions above the energy gap  $E_g$ .  $\delta(x)$  and  $\theta(x)$  are the Dirac-delta and the Heaviside step function, respectively, and  $E_b$  is the exciton binding energy.

Eq. (1) can be used to fit the measured absorption spectra of perovskite films, provided that it is convoluted with a bell-shaped function accounting for line broadening. In addition, the introduction of the joint valence-band energy-momentum dispersion leads to a better approximation between theory and experiment, as it overcomes the limits of the parabolic bands approximation. Upon these improvements, Eq. (1) can be modified as follows:

$$\alpha(\hbar\omega) = \frac{\alpha_{\text{scal}}}{\hbar\omega} \left[ \sum_j \frac{2E_b}{j^3} \operatorname{sech}\left(\frac{\hbar\omega - E_j^b}{\Gamma}\right) + \int_{E_g}^{\infty} \operatorname{sech}\left(\frac{\hbar\omega - E}{\Gamma}\right) \frac{1}{1 - e^{-\frac{2\pi\sqrt{E_b}}{E - E_g}}}} \left[ 1 + \frac{10\mu b}{\hbar^4} (E - E_g) \right] dE \right] \quad (2)$$

The density of states has been developed in series at the first order for small values of  $b$ , which is a factor that takes into account the non-parabolic dispersion. The hyperbolic secant function of width  $\Gamma$  accounts for thermal and inhomogeneous broadening;  $\alpha_{\text{scal}}$  is a constant that is adjusted in order to obtain the right scaling between the model and the experimental absorption spectrum; in the fitting procedure, we also allowed for absorbance offsets often found in experimental curves due to unbalanced reference or zero spectra in spectrophotometers.

In order to establish that the model can describe the absorption of MAPbI<sub>3</sub> perovskite films, regardless of the particular morphology and growth conditions of each sample, we fitted Eq. (2) with a least square method to several absorption spectra reported in literature by different research groups. The binding energy is obtained as a fitting parameter, and the fitting range has been extended as much as possible at low and high energy in order to minimize uncertainties connected to the calculation procedure. Published data were extracted from the pdf files through the CurveSnap software, freely available online.

First, we analyzed the absorption measurements at low temperature, where the broadening is less pronounced and therefore the fitting procedure is more sensitive to the value of the exciton binding energy. Figures 1a,b show a comparison between the absorption spectra reported by D'Innocenzo et al. and our experimental data, recorded at 160 and 170 K, respectively [22,30]; the relative contributions of excitons and free carriers to the absorption spectrum are also shown. While the broadening is different in the two cases, the values of the exciton binding energy are comparable and coincide within the uncertainty. Figures 1c–f show the same analysis carried out at room temperature, applied to absorption spectra reported in references [5,22,45]. Even at room temperature, the fitted values for  $E_b$  do not differ more than 20% from the average of 23 meV. Such value is intermediate between the binding energy typical of Frenkel excitons in organic semiconductors (>100 meV) and the one typical of Wannier excitons in inorganics (<10 meV) [46,47].

The overall picture emerging from the analysis of optical absorption data seems therefore converging towards a value of 23 meV for the exciton binding energy. These results are in contrast with what observed with magnetometry, as some recent publications have reported values of the exciton binding energy that depend on temperature, as a consequence of screening effects. Such works report exciton binding energy to be nearly 15 meV at low

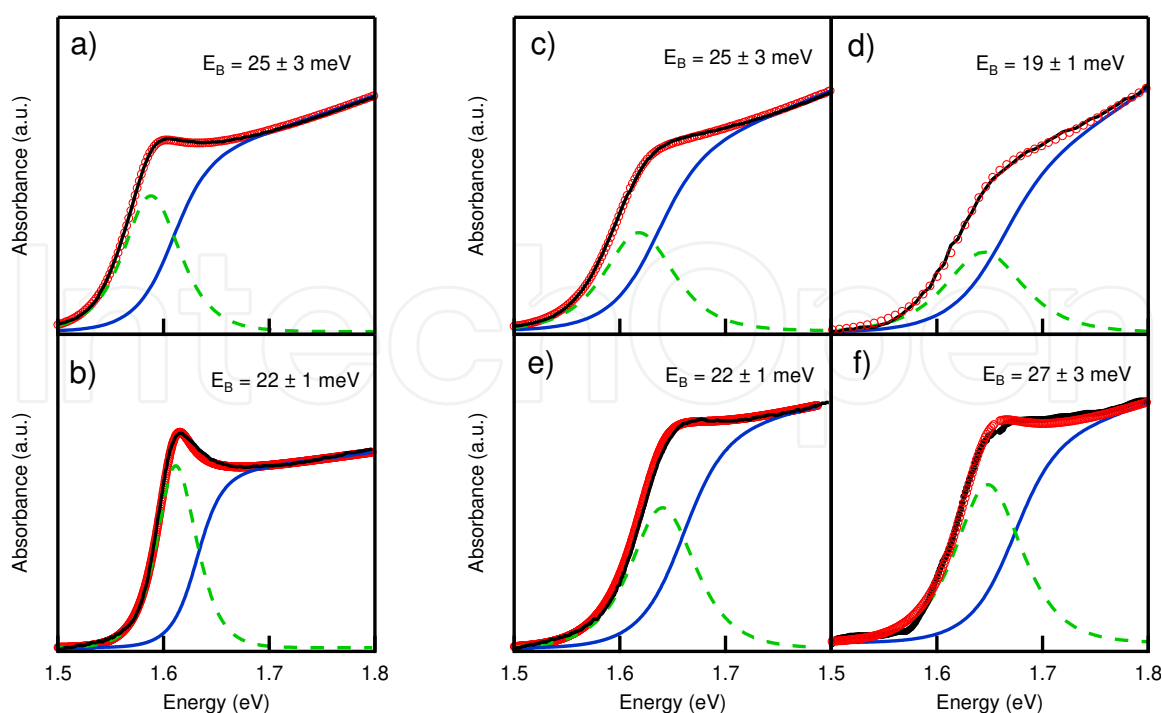


**Figure 1.** Absorption spectra in MAPbI<sub>3</sub> perovskite films. The red empty circles represent the theoretical fits to the experimental data (continuous black lines). The contributions to the absorption due to both excitonic and band-to-band transitions are modelled in the framework of the Elliott's theory of Wannier excitons. The dotted green lines are relative to excitonic transitions, while the continuous blue lines are relative to band-to-band contributions with the inclusion of Coulomb interactions between electrons and holes. (a,b) Absorption spectrum reported by Saba et al. at 170 K and by D'Innocenzo et al. at 160 K, respectively [22,30]. (c,d,e,f) Absorption spectra reported at room temperature by Saba et al., Sutherland et al., D'Innocenzo et al. and Stranks et al., respectively [5,22,30,45].

temperature and a few meV at 300 K [33,34,38,48], while previous works with similar techniques reported values as large as 50 meV [31,49]. Since the interpretation of magnetometry data requires several analysis steps, at the moment it is not clear what the origin of this discrepancy is.

### 3. Emission properties from free carriers

Linear absorption spectroscopy is extremely useful to obtain information about the optical response and quickly highlights benefits and disadvantages of the material in terms of light harvesting, which represents the main ingredient for photovoltaics applications. Further insight into the electronic properties is provided by the study of the excited state emission properties, as the techniques probe how optical excitations populate the available states. Particularly, photoluminescence under pulsed, femtosecond excitation is useful in determining relaxation rates and excited state dynamics.

Emission in MAPbI<sub>3</sub> and MAPbI<sub>3-x</sub>Cl<sub>x</sub> perovskites occurs close to the excitonic resonance and the high energy side of the PL peak overlaps with the continuum of band-to-band transitions

in a wide excitation range, as shown in Figure 2a. Short-pulse excitation experiments show that the PL signal rises instantaneously after the laser pulse arrival; the time decay of photoluminescence can be observed from Figures 2b,c. Two different samples are presented, MAPbI<sub>3</sub> and MAPbI<sub>3-x</sub>Cl<sub>x</sub> perovskites; absorption and emission properties are quite similar in both perovskites, since chlorine content has been determined to be a small fraction, not larger than 2%. However, the dynamics of the PL is different in the two samples, with much longer decay in the MAPbI<sub>3-x</sub>Cl<sub>x</sub> film; several reports in literature state that the role of Cl is to alter the perovskite crystallization dynamics and, as a result, MAPbI<sub>3-x</sub>Cl<sub>x</sub> perovskites have lower trap densities than what observed in MAPbI<sub>3</sub> [50,51], with a corresponding longer excited state lifetime. Inset in Figure 2a shows a clear difference between perovskites with and without chlorine in terms of PL lifetimes at low laser intensity, according to what reported in literature.

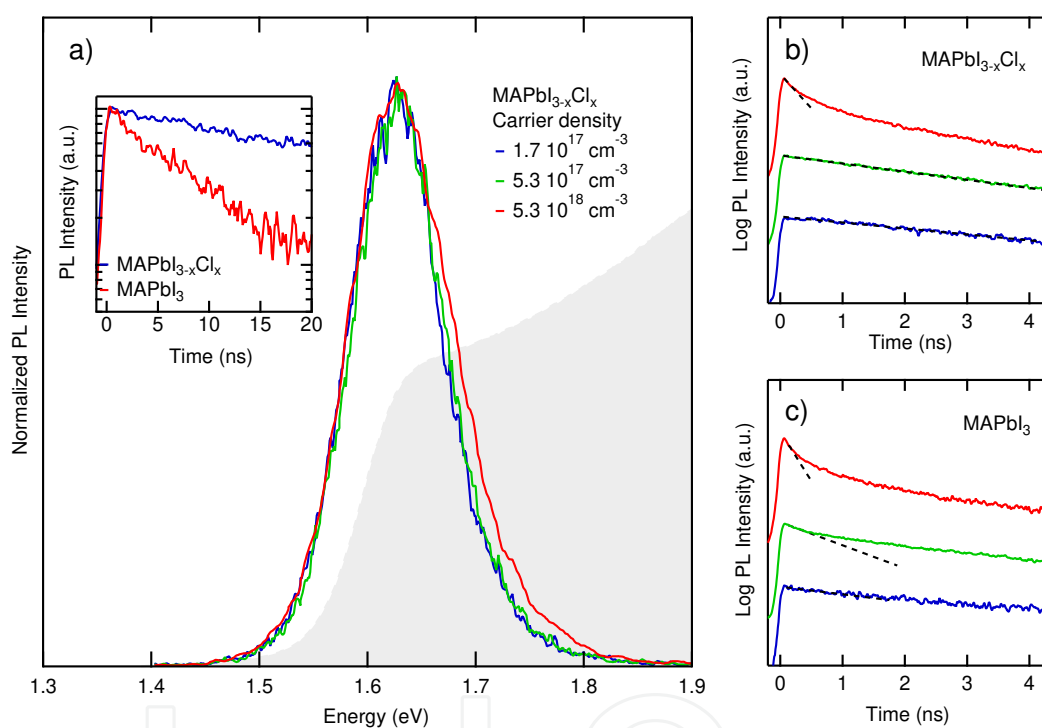


**Figure 2.** (a) Transient photoluminescence spectra for mixed MAPbI<sub>3-x</sub>Cl<sub>x</sub> films at 300 K, integrated in 60 ps (temporal resolution of our streak camera), compared with the absorption spectrum at the same temperature (gray shadow). Photoluminescence was excited by 130-fs-long laser pulses with a repetition rate of 1 kHz and 3.18 eV photon energy. The legend reports the injected carrier density, calculated from laser pulse fluence and film absorbance. Inset: time resolved PL signal from mixed MAPbI<sub>3-x</sub>Cl<sub>x</sub> (blue line) and pure MAPbI<sub>3</sub> (red line) films, relative to an excitation density of at 1.7 × 10<sup>17</sup> cm<sup>-3</sup>. The different mean PL lifetime is attributed to different trap densities in the samples. (b,c) Transient PL signal as a function of the injected electron-hole pair density at the film surface in MAPbI<sub>3-x</sub>Cl<sub>x</sub> (b) and MAPbI<sub>3</sub> films (c). The initial decays of the signal are fitted by an exponential function (black dotted lines). The injected carrier densities are relative to the PL spectra shown in (a).

Radiative recombination processes can be investigated studying the intensity of the photoluminescence signal immediately after the laser excitation (PL<sub>0</sub>), before electronic states are depopulated by slow recombination mechanisms. The electron-hole pair density  $n_0$  at the sample surface, injected from a short laser pulse, can be estimated multiplying the laser pulse

fluence times the absorption coefficient of the sample at the excitation wavelength. The evolution of  $PL_0$  with  $n_0$  shows what type of carrier prevails as outcome of the photoexcitation.

Figure 3 shows  $PL_0$  as a function of  $n_0$  in  $MAPbI_3$  and  $MAPbI_{3-x}Cl_x$  perovskites. The PL intensity scales quadratically in the injected carrier densities from less than  $10^{16}$  to  $10^{18}$   $cm^{-3}$ , which corresponds to laser pulse fluence values from less than 0.1 to about 10  $\mu J/cm^2$ . Such quadratic scaling is the signature of bimolecular recombination and is consistent with the radiative recombination from a gas of unbound electron-hole pairs [52]. On the other hand, isolated excitons should give rise to monomolecular recombination, with the  $PL_0$  intensity linear in the exciting laser fluence.  $PL_0$  tends to saturate above  $2.5 \times 10^{18}$   $cm^{-3}$ , as a consequence of the band filling.

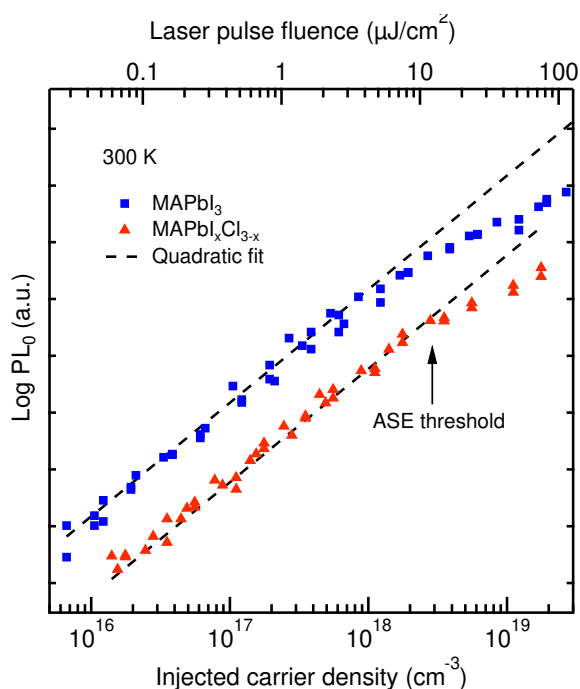


**Figure 3.**  $MAPbI_3$  and  $MAPbI_{3-x}Cl_x$  photoluminescence emission intensity estimated at  $t=0$  ( $PL_0$ ) as a function of injected electron-hole density (lower axis) and laser pulse fluence (upper axis).  $PL_0$  values relative to laser pulse fluences higher than 100  $\mu J/cm^2$  could not be extracted from experimental decays, since they were much faster than the temporal resolution of our instrument. The black-dashed lines represent the  $PL_0$  quadratic dependence on  $n_0$ , and are reported as a guide for eyes.

Focusing only at time zero, all the recombination processes that occur later after laser excitation are neglected. On the other hand, they can be investigated studying the quantum yield (QY), defined by the ratio between the time-integral of the PL signal (TIPL) and the laser fluence  $\phi$ .

Figure 4a shows the QY as a function of the laser fluence, which can be explained in terms of interplay between radiative and non-radiative recombination processes. The rise of the QY below  $n_0 \sim 10^{17}$   $cm^{-3}$  is due to the fact that carrier trapping is the fastest recombination process in such excitation regime, while radiative recombination becomes faster for growing carrier

densities, so that a larger fraction of optical excitations recombine radiatively. The increase in QY reaches a maximum above  $n_0 \sim 10^{17} \text{ cm}^{-3}$ , as the radiative recombination rate overcomes the carrier trapping and becomes the fastest recombination channel; under such conditions, a further increase in the radiative recombination rate only makes recombination faster, but it does not significantly increase the fraction of carriers that recombine radiatively, which is already close to unity. For even higher excited densities, above  $n_0 \sim 10^{17} \text{ cm}^{-3}$ , non-radiative density-dependent Auger recombination, whose rate is cubic in the density, and therefore increases faster than the radiative rate, becomes dominant, causing the observed QY decrease [30]. The remarkable high values of the QY (30% for MAPbI<sub>3</sub> and 70% for MAPbI<sub>3-x</sub>Cl<sub>x</sub>) are reached for injected carrier densities close to the amplified spontaneous emission thresholds reported for these materials [18,19].

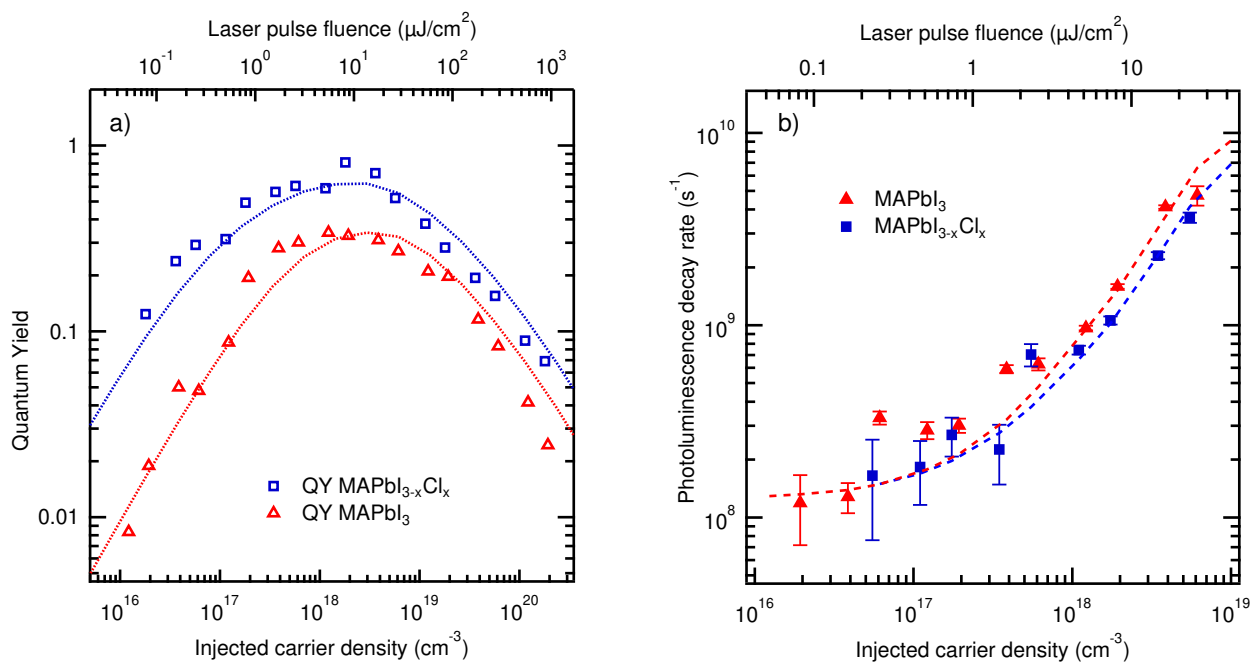


**Figure 4.** Photoluminescence quantum yield and photoluminescence decay rates for the two perovskite samples (MAPbI<sub>3</sub> red triangles, MAPbI<sub>3-x</sub>Cl<sub>x</sub> blue squares). (a) The emission quantum yields are calculated as  $\text{TIPL}/\phi$ , where  $\phi$  is the laser pulse fluence. The injected carrier density is calculated multiplying the laser pulse photon fluence by the absorption coefficient of the films. As a reference, the laser pulse fluence directly measured in the experiments is also reported on the top axis. Initially, the QY grows with fluence for both films, as the bimolecular recombination becomes faster and a growing fraction of the injected excitations recombine radiatively, instead of being trapped. At excitations  $4 \times 10^{19} \text{ cm}^{-3}$ , non-radiative Auger processes dominate. The absolute QY is scaled to match theoretical predictions. The maximum QY values are about 30% for MAPbI<sub>3</sub> and 70% for MAPbI<sub>3-x</sub>Cl<sub>x</sub>. The dotted lines represent predictions from a rate equation model accounting for the main relaxation channels for electrons and holes. Simulations take into account the exponential spatial profile of the electron-hole density created by laser pulses. The very good agreement between model and data indicates that the main photophysical processes are accounted for in the model. (b) Decay rates for the transient PL signal plotted as a function of the injected carrier density on bottom axis and the laser pulse fluence on top axis. The rates, defined as  $k_{\text{PL}} = \left[ \frac{d\text{PL}}{dt} \cdot \frac{1}{\text{PL}} \right]_{t=0}$  are extracted from the data in Figures 2b,c. Such rates represent the initial decay and should not be mistaken for the average photoluminescence decay rate obtained by fitting the entire decay with an exponential function. The error bars represent the standard deviation from a least square fit to an exponential decay and are reported only when they exceed the size of the marker. The rates are very similar

for the two samples (although the average exponential decay rates are significantly different) and grow together for growing injected carrier densities. Such rates measure the intrinsic density-dependent bimolecular and Auger recombination processes. The dotted lines represent the results of the rate equation used to model the experimental data: the agreement with the experiment is satisfactory also in this case.

Also the analysis of the initial PL decay rate at time zero, extracted right after laser pulse excitation, confirms our interpretation of the hierarchy of the recombination rates. Figure 4b shows that the initial PL decay rate increases with  $n_0$ , as a consequence of the activation of density-dependent recombination mechanisms. Differently from the average PL decay rate, calculated at low excitation intensity, which is different in various samples (inset in Figure 2a), the initial PL decay rate is quite similar among them. This fact reflects that while the mean PL decay time is sensitive to extrinsic effects like traps and defects, which are significant in all solution-processed semiconductors, the initial PL decay rate is dictated only by intrinsic nonlinear processes [30]. For growing excitation densities, the initial recombination rates increase in both perovskite samples, as radiative and Auger recombination become faster and faster.

#### 4. Recombination rates

Fundamental parameters of semiconductors can be estimated theoretically by analyzing absorption and photoluminescence experimental results. As well as the absorption coefficient and the emission wavelength, bimolecular and Auger recombination rates represent two constants that characterize the material and can be used as figures of merit for some optoelectronic applications. Values of the bimolecular recombination constant from  $10^{-11}$  to  $10^{-9}$   $\text{cm}^3 \text{s}^{-1}$  have been reported in literature for  $\text{MAPbI}_3$  and  $\text{MAPbI}_{3-x}\text{Cl}_x$  perovskites [20,30,53]. One would expect that for such an intrinsic process similar values are to be obtained in all samples. Such wide range of reported values can be attributed to the different methods used to calculate it. It is common to extract the bimolecular constant from the PL decay curves, fitting them to a multi-power decay. Such method, however, does not provide reliable estimates whenever applied to noisy curves with several competing processes that are simultaneously relevant; in the particular case of perovskites, a monomolecular decay from trapping, a bimolecular one from radiative recombination and trimolecular one for Auger need to be accounted simultaneously, all convoluted with the temporal resolution of the experimental apparatus. On the other hand, extracting the bimolecular constant from the absorption coefficient is a widely used method in solid state physics that makes use of the symmetry between absorption and emission processes and is completely independent on non-radiative recombination processes. In order to extract the bimolecular coefficient, one has to fit the absorption spectrum with the Kubo-Martin-Schwinger relation, as detailed in references [54,55]. Our estimate of the bimolecular constant in  $\text{MAPbI}_3$  perovskites, extracted from absorption, is  $2.6 \times 10^{-10} \text{ cm}^3 \text{s}^{-1}$ , a value included between the two extrema reported in literature.

Differently from the bimolecular constant, the Auger recombination rate could significantly change among samples, as it increases with the defect density of a crystal, which can depend on the synthesis method and the surface morphology [56,57]. Recent works report Auger

recombination constants from  $10^{-29}$  to  $10^{-28} \text{ cm}^6 \text{ s}^{-1}$  for pure and mixed methylammonium lead iodide perovskites. Our estimates of  $2 \times 10^{-28} \text{ cm}^6 \text{ s}^{-1}$  for  $\text{MAPbI}_{3-x}\text{Cl}_x$  and  $4 \times 10^{-28} \text{ cm}^6 \text{ s}^{-1}$  for  $\text{MAPbI}_3$  perovskites are consistent with other published results [20,30]. Auger recombination rate is higher in pure iodide perovskites than in those with chlorine, according to the less crystallinity in samples synthesized without Cl.

## 5. Steady-state photoluminescence

The experimental results obtained under impulsive regime have provided numerical estimates of fundamental parameters in perovskites and a clearer view of the excited state dynamics. Nevertheless, such kinds of experiments do not investigate what occurs when samples are continuously excited and there is interplay between absorption and relaxation processes, as happens in steady-state operation. In perspective of the realization of perovskite-based working devices, it is important to have a deep understanding of these processes, as real devices work under continuous operation. A reliable instrument of investigation of the steady-state properties is represented by experiments carried out exciting samples under cw pumping or with pulses much longer in time than the PL lifetime of the excited states.

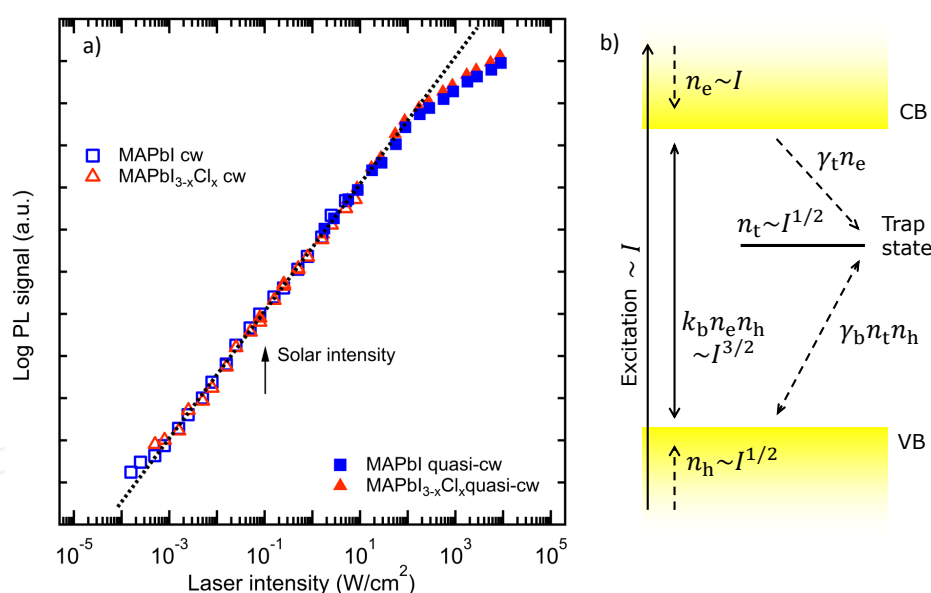


**Figure 5.** Steady-state photoluminescence. (a) Photoluminescence signal as a function of the intensity of the exciting laser. The empty markers represent the measurements obtained with a cw Nd:Yag 532 nm laser; the filled markers are instead measured in quasi-cw conditions, exciting the samples with 300-ns-long laser pulses from a Q-switched 527 nm Nd:Ylf laser; the pulse duration is much longer than all the relevant relaxation rates, so that steady-state conditions are expected to be achieved during laser excitation. The PL signal grows as  $I^{3/2}$  for a wide range of excitations. Investigations were extended from laser intensities much lower than the solar one to intensities large enough to generate population inversion and optical gain. The unusual  $3/2$  power law is attributed to intra-gap trap states with only electrons or only holes, but not both of them. The dashed black line shows the PL dependence in laser intensity as a result of the trap model, under the assumption that electrons are the trapped species. (b) shows a sketch of the relaxation of optical excitations under steady-state conditions (VB is the valence band and CB the conduction band).

Figure 5a shows our experimental results carried out under cw excitation, spanning light intensities from  $10^{-4}$  to  $10^4$  W/cm<sup>2</sup>. Below 100 W/cm<sup>2</sup>, the PL signal follows a 3/2 power law in the laser intensity for five decades excitation intensity. Such 3/2 power dependence implies that the radiative recombination is not the only process that governs the electron-hole dynamics under this regime; otherwise a linear dependence of the PL in the laser intensity would be expected, if radiative processes would be dominant. The particular 3/2 power law could be explained accounting the role of intra-gap states that act only on one kind of carrier, meaning traps only for electrons or only for holes (Figure 5b). Above  $10^2$  W/cm<sup>2</sup>, the deviation from the 3/2 power law to a linear dependence is attributed to the increase of radiative recombination with respect to carrier trapping [30]. Trap density is estimated to be of the order of  $10^{16}$ - $10^{17}$  cm<sup>-3</sup>, in agreement with what reported by other works [6]. Despite such large trap density, carrier trapping does not prejudice electronic properties, as PL lifetimes exceed several nanoseconds from intensities smaller than solar illumination to those typical to obtain light amplification. Hence, the resulting carrier mobility is sufficiently high to justify the remarkable transport properties and the efficient charge collection in perovskite-based solar cells reported in literature.

## 6. Organolead halide perovskites as active media in laser devices

The strong absorption at the band-edge, in addition to the ambipolar transport with high carrier mobility and gap-tunability, makes organometal halide perovskites very promising not only for the realization of solar cells but also as optical gain media in laser devices, as highlighted by many reports showing amplified spontaneous emission under intense photoexcitation [17–19,39,45,58]. Deschler et al. and Xing et al. reported optically pumped lasing and amplified spontaneous emission from perovskites arranged in cavity resonators and in cavity-free configuration, respectively [17,18]. Recently, Zhu et al. reported threshold densities of the order of  $10^{16}$  cm<sup>-3</sup> from single-crystal lead halide perovskite nanowires, which is a value about two orders of magnitude smaller than what was reported by the previous works [39]. In the light of these results, it is clear that organometal halide perovskites have a potential application as active media in laser devices. However, demonstrations reported up to date report ASE under impulsive excitation, a condition well away from real laser devices, which work under continuous operation. Probing emission properties with ns-long-pulse excitation simulates a regime more similar to what happens in a real device, and provides further information about the potentialities and the shortcomings of perovskites as optical gain media [19]. The first report about nanosecond excitation is the one published by Sutherland et al., which shows lasing from MAPbI<sub>3</sub> perovskite thin layers deposited on spherical glass resonators, exciting samples with 2-ns-long pulses [45]. Nevertheless, this regime is still far from a real cw excitation and other experiments are required to have a deeper understanding of emission properties in perovskites [19]. Results obtained in different excitation regimes, from the impulsive to the quasi-cw, and improvements of our experiments with respect to other works are reported in the following sections and compared with the most recent researches.

## 7. Lasing and ASE under impulsive excitation

ASE in MAPbI<sub>3</sub> and MAPbBr<sub>3</sub> perovskite thin films manifests itself through a sharp peak that appears under short-pulse excitation in the low energy side of the PL spectrum of both films, when the injected carrier density reaches a threshold value. Figure 6 shows emission spectra at different excitation intensities from methylammonium iodide and bromide perovskite thin films at room temperature.

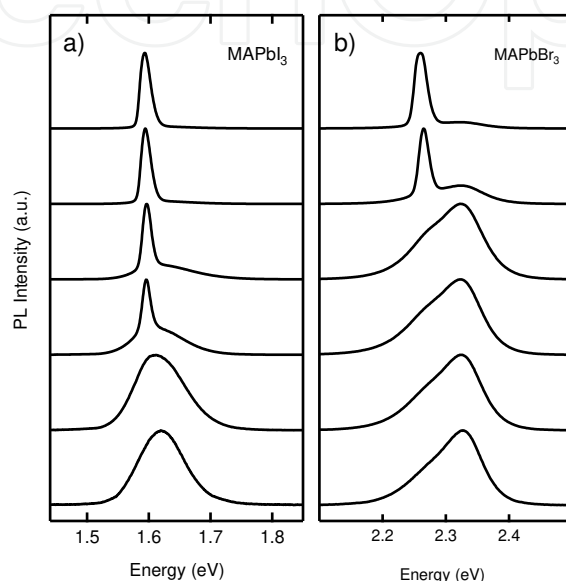


**Figure 6.** Time integrated photoluminescence spectra of MAPbI<sub>3</sub> (a) and MAPbBr<sub>3</sub> (b) perovskites at 300 K. Emission was excited by 130-fs-long laser pulses with a repetition rate of 1 kHz and 3.18 eV photon energy. Spontaneous and amplified spontaneous emissions were detected by a CCD camera. From top to bottom: laser fluence = 90  $\mu\text{J}/\text{cm}^2$ , 70  $\mu\text{J}/\text{cm}^2$ , 40  $\mu\text{J}/\text{cm}^2$ , 30  $\mu\text{J}/\text{cm}^2$ , 20  $\mu\text{J}/\text{cm}^2$ , 10  $\mu\text{J}/\text{cm}^2$ .

ASE threshold densities are calculated by averaging the laser fluence times the absorption coefficient at the excitation wavelength over the film thickness. Even if samples realized with the same procedure are excited with the same laser source, they show slightly different values of the ASE threshold, but for most samples the threshold is in the interval  $2\text{--}5 \times 10^{18} \text{ cm}^{-3}$  [19]. Such values are comparable to the ones reported by Xing et al. ( $1.7 \times 10^{18} \text{ cm}^{-3}$  in MAPbI<sub>3</sub> films), who investigated MAPbX<sub>3</sub> (where X = Cl, Br, I) thin films under short-pulse excitation [18]. The dispersion of the ASE thresholds among the same set of samples can be attributed to their surface morphology, which is the main responsible for optical losses. Instead, the large difference in ASE values reported in various publications can be associated to the sample architecture, in addition to the issues originated from the surface morphology. In the experiments reported by Deschler et al., MAPbI<sub>3-x</sub>Cl<sub>x</sub> perovskite layers were placed between dielectric and evaporated gold top mirrors [17]. The same perovskite layers show ASE in cavity-free configuration, but at fluences above 1 mJ/cm<sup>2</sup>, about two orders of magnitude higher than what observed in both our results and the ones reported by Xing et al. [18]. The remarkable low lasing thresholds reported by Zhu et al. ( $1.5 \times 10^{16} \text{ cm}^{-3}$ ) are attributed to both

the high crystallinity of nanowires and their morphology, as the linear shape of nanowires acts as waveguide [39].

Even though such investigations are extremely useful in perspective of the realization of a perovskite-based laser, they are not sufficient to state if these materials could be effectively employed as optical gain media. Actually, experiments carried out under impulsive regime do not take into account any interplay between laser excitation rates and relaxation processes that occur in real cw lasers, as the carrier injection is ultrafast and the emission occurs immediately after, when pumping has already stopped. Real lasers work under cw operation, a more complicated condition than what happens under impulsive regime, as excitation and emission occur at the same time and optical amplification is observed until the population inversion condition is kept. Under cw excitation, issues connected to warming could considerably affect the light emission properties, especially at high-injected carrier densities (above  $10^{18} \text{ cm}^{-3}$ ), where non-radiative Auger recombination begins to compete with optical emission [19,30].

## 8. Amplified spontaneous emission under ns excitation

Investigation of emission properties under excitation pulses having duration comparable or longer than the PL lifetime supplies the limits of the ultrafast pumping. Under 4-ns long-pulse excitation, ASE is observable at room temperature in both  $\text{MAPbI}_3$  and  $\text{MAPbBr}_3$  thin films at threshold densities of the order of  $10 - 15 \text{ kW/cm}^2$  ( $\sim 40 - 60 \mu \text{ J/cm}^2$ ) [19]. Such values are comparable with what reported by Sutherland et al. ( $65 \pm 8 \mu \text{ J/cm}^2$ ), who excited perovskite layers of  $\sim 75 \text{ nm}$  in thickness with pulses of 2 ns [45]. At this excitation intensity, the PL lifetime of our samples, measured under femtosecond laser excitation, is about 1 ns, which is a value lower than the 4-ns laser pulse.

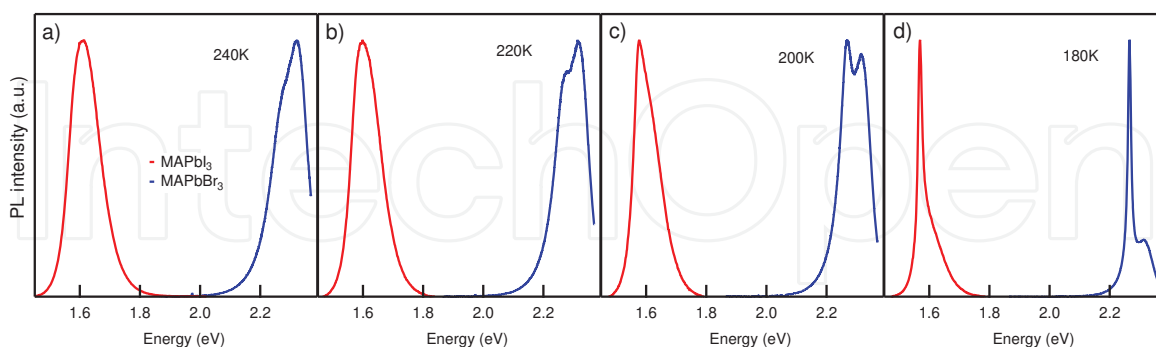


**Figure 7.** Quasi-steady-state stimulated emission in trihalide perovskite films. Photoluminescence was excited at different temperatures by 300-ns-long laser pulses with a repetition rate of 6 Hz and 2.35 eV photon energy. (a–d) Time-integrated photoluminescence spectra of  $\text{MAPbI}_3$  (red lines) and  $\text{MAPbBr}_3$  (blue lines) perovskites detected by a CCD camera; ASE occurs at cryogenic temperatures (180 K), but disappears around 220 K.

Despite using excitation pulses of 4 ns could be considered a quasi-cw excitation regime, such pumping is not sufficient to guarantee if perovskites can act as active media in a real device.

Using 300-ns-long pulses as laser source, no ASE is observed at room temperature in any perovskite film. A very small hint of amplification is observed at 220 K and a clear ASE peak appears at lower temperatures, as can be observed from Figure 7. Such findings suggest that some processes connected to temperature clearly affect the ASE threshold density under cw excitation. ASE inhibition is likely due to the higher amount of energy deposited by the long pulses, which results in more warming than what obtained under short-pulse excitation [19].

## 9. Optical thermometry

The plasma temperature can be extracted from PL spectra by fitting the high energy tail of the emission peak to a  $Ae^{-E/k_B T_p}$  Boltzmann function, where  $A$  is an arbitrary multiplication factor,  $E$  the photon energy,  $k_B$  the Boltzmann constant and  $T_p$  the plasma temperature [59].

Inset in Figure 8 illustrates the fitting procedure and shows the plasma temperature as a function of the laser fluence. As one may expect, the plasma temperature increases for increasing laser fluence. The main plasma heating sources under photoexcitation are due to the excess energy of the laser photons with respect to the energy gap and to non-radiative processes from both carrier trapping (at low intensities) and Auger recombination (at high intensities) [19]. Sample excitation with different laser wavelengths, from energies higher than the energy gap to about resonant with it, shows direct effects of excess energy on plasma temperature. Experimental results, reported in Figure 8, show that both contributions are significant, as larger excess energy causes larger warming, but some warming occurs even for quasi-resonant excitation, when Auger is the main source of heating. The role of Auger recombination is also evident at high densities by the rapid increase of the plasma temperature with the excitation intensity.

More significant warming effects can be observed using 300-ns-long excitation pulses and measuring the time-resolved PL evolution at different lattice temperatures  $T_L$  and, for each  $T_L$ , at different excitation intensities. Here, the thermometry is applied to each of the spectra in the time-resolved spectrogram and therefore yields information about the temporal dynamics of the plasma temperature. At low excitation intensities, the time-resolved PL signal follows instantaneously the laser pulse, while for densities comparable and higher than ASE threshold, a clear temporal reshape of the PL signal is observed. Such process is evident at high laser intensity even when ASE is not noticeable from PL spectra as shown in Figure 9c,d. The temperature dynamics helps providing a physical explanation, showing that the temporal reshape is accompanied by an increase in the plasma temperature.

Both the temporal reshaping and the observation of ASE only at low lattice temperature under long-pulse excitation can be interpreted in terms of decrease of the radiative efficiency with increasing laser intensity. Such process is a consequence of the plasma warming generated during the intense pulse [19]. An interesting point is that every time ASE is observed, it stops when the plasma temperature overcomes about 370 K, independently from the initial temperature of the lattice (Figures 9e,f).

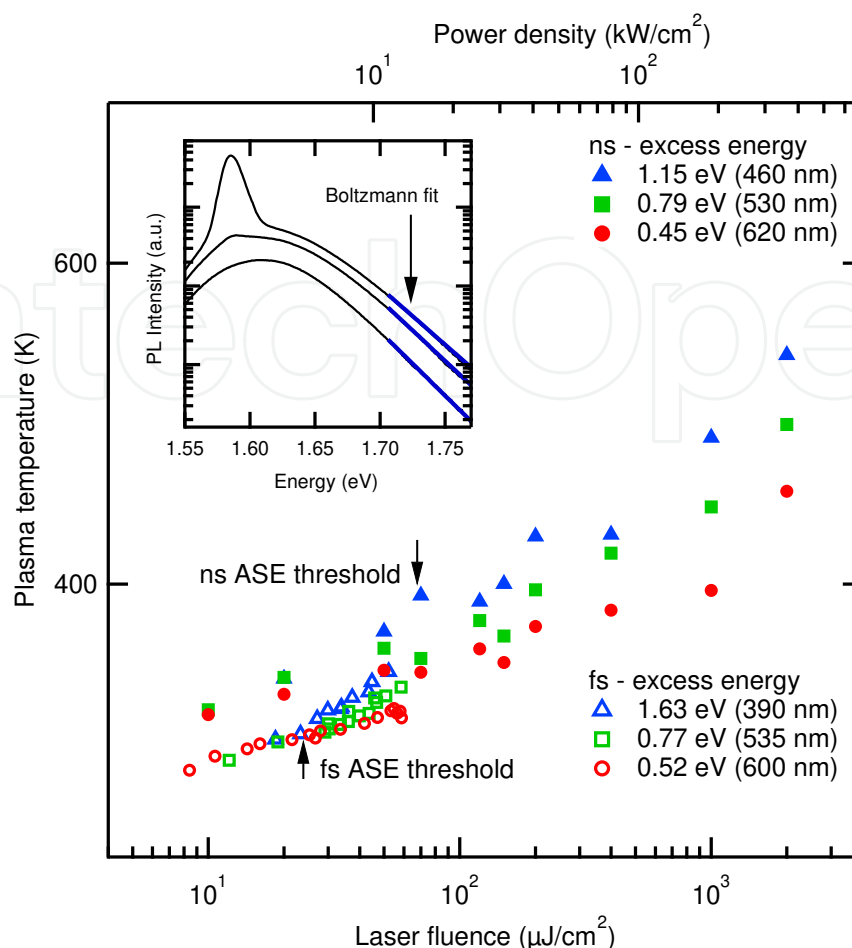


**Figure 8.** Plasma temperatures of a MAPbI<sub>3</sub> film as a function of the laser fluence. The empty markers represent the measurements obtained exciting the sample at a lattice temperature of 300 K with 130-fs-long laser pulses at repetition rate of 1 kHz and different photon energies; the filled markers represent the opposite regime, with 5-ns-long laser pulses at a repetition rate of 10 Hz and different photon energies. The arrows represent the ASE thresholds for the two excitation regimes. The corresponding average excitation power density during the ns laser pulses is also reported on the top axis as a reference; such axis does not apply to measurements under fs excitation. The excess energy was calculated as the difference between the excitation photon energy and the energy gap (1.55 eV); the wavelength indicated in brackets is the actual central wavelength of the excitation laser. Inset: plasma temperatures are extracted fitting the high energy tail of photoluminescence spectra with a  $Ae^{-E/k_B T_P}$  exponential function, representing a Boltzmann thermal distribution,  $E$  being the photon energy,  $T_P$  the temperature,  $k_B$  the Boltzmann constant and  $A$  an arbitrary multiplication factor. The blue lines represent the fitting functions.

As a confirmation, one can measure the ASE threshold densities carried out under short-pulse excitation as a function of the lattice temperature, from 300 K to 160 K. Experimental results, reported in Figure 10, show that ASE threshold fluence follows a quadratic dependence in the lattice temperature in both MAPbI<sub>3</sub> and MAPbBr<sub>3</sub> perovskites [19]. Since absorption does not change significantly from room temperature to 160 K, such dependence cannot be ascribed to a variation of the injected electron-hole pairs density with temperature, but to the influence of temperature on the radiative recombination rate. Indeed, it is known that the radiative rate of an electron-hole plasma is inversely proportional to the plasma temperature [52].

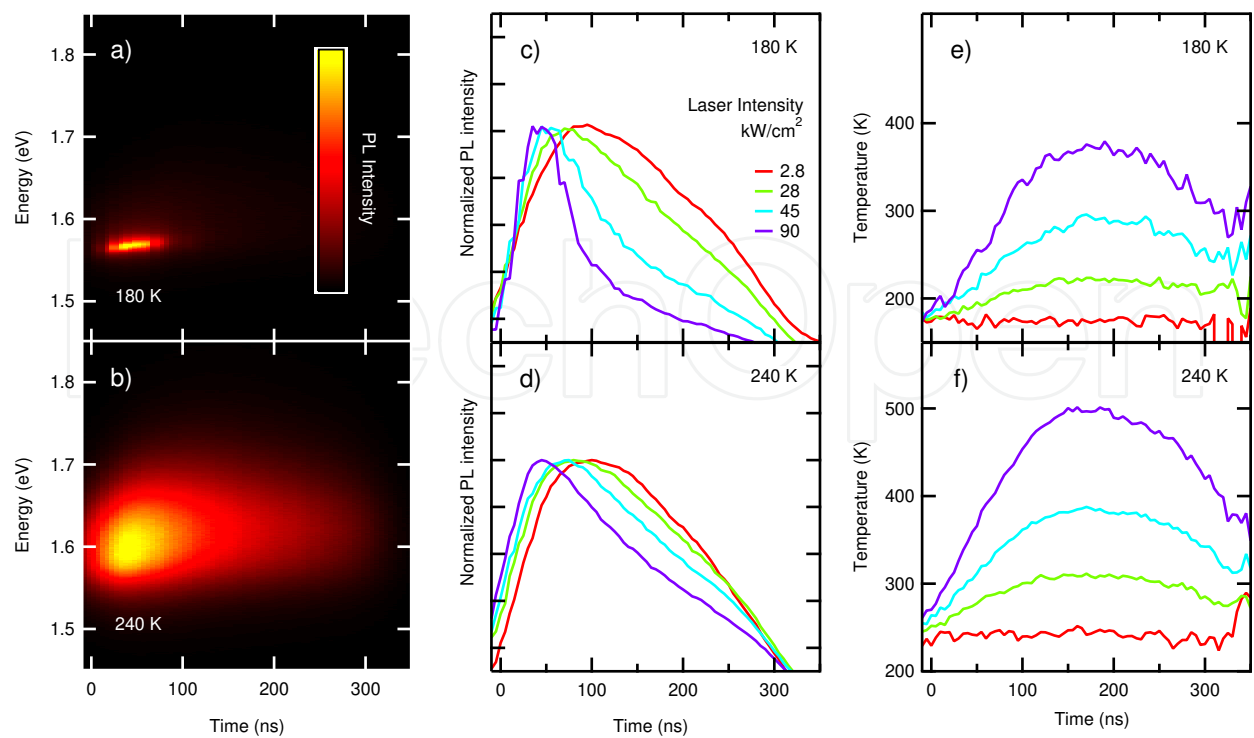


**Figure 9.** Photoluminescence was excited at different lattice temperatures by 300-ns-long laser pulses with a repetition rate of 6 Hz and 2.35 eV photon energy. (a,b) Time-resolved PL spectrograms of a MAPbI<sub>3</sub> film, acquired with a gated intensified camera at different lattice temperatures. (c,d) Corresponding PL temporal profiles, which demonstrate a narrowing of the emission profile with respect to the exciting laser pulse duration; we attributed the effect to stimulated emission and Auger recombination. (e,f) Plasma temperature extracted from MAPbI<sub>3</sub> photoluminescence spectrograms in panels a,b, at different lattice temperatures, with the fitting procedure reported in the inset of Figure 8. Significant warming occurs during the excitation pulse and limits the duration of ASE.

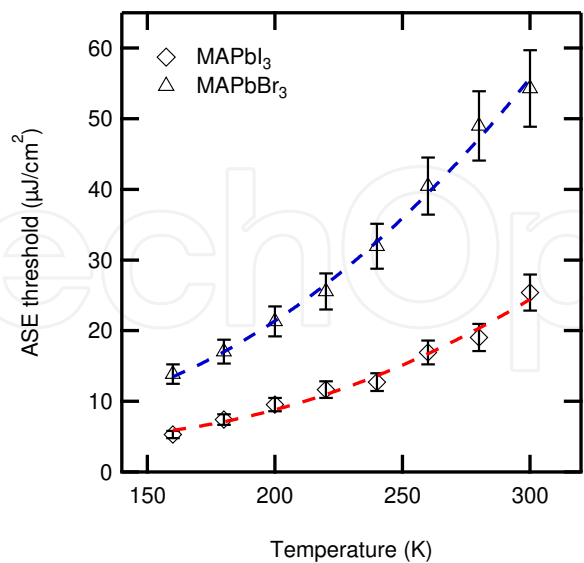


**Figure 10.** ASE threshold fluence as a function of the lattice temperature in MAPbI<sub>3</sub> and MAPbBr<sub>3</sub> perovskites, under short-pulse excitation. The dashed lines are fits of measured values to a quadratic dependence of the ASE threshold on temperature.

## 10. Comparison with nitride semiconductors

Table 1 compares the values of parameters relevant to optical amplification obtained for perovskites to those known for nitride semiconductors at room temperature. Such comparison is very instructive in perspective of the realization of a perovskite-based cw laser. In fact, the advancement of nitride-based lasers has overtaken the problems concerning warming with success and may serve as a useful guide to improve perovskite device performances.

	$n_{\text{thr}} (\text{cm}^{-3})$	$\tau_{\text{thr}} (\text{ns})$	$\gamma_A (\text{cm}^6 \text{s}^{-1})$	$R_{\text{th}} (\text{K kW}^{-1} \text{cm}^2)$
Perovskites [18,19,39,60]	$10^{16}\text{-}10^{18}$	1-3	$4 \times 10^{-28}$	2-4
Nitrides [61]	$10^{18}\text{-}10^{19}$	2-5	$5 \times 10^{-30}$	0.5

**Table 1.** Comparison between perovskites and nitrides ASE threshold density  $n_{\text{thr}}$ , lifetime at ASE threshold  $\tau_{\text{thr}}$ , Auger recombination constant  $\gamma_A$  and thermal resistance  $R_{\text{th}}$  respectively. Values are relative to room temperature.

It can be observed that  $\tau_{\text{thr}}$ , that is, the carrier lifetime at ASE threshold density, is slightly longer in nitrides than in perovskites, thanks to the significantly lower value of the Auger recombination coefficient  $\gamma_A$ , which has a value almost two orders of magnitude smaller than in perovskites. Auger recombination is the major responsible for the efficiency reduction in nitride-based LEDs at high power and the value of  $\gamma_A$  is higher in the presence of disorder due to defects [56,57]. It is therefore important to reduce the Auger recombination coefficient in perovskites, for example, acting in order to decrease both the trap density and the ASE threshold, for example, improving the crystallinity and the surface morphology quality. Another crucial parameter is the thermal resistance  $\gamma_A$ , which is about four to eight times higher in perovskites than in nitrides. Furthermore, the substrate on which perovskites are deposited could seriously contribute to enhance the value of the thermal resistance, thus increasing the ASE threshold, particularly under long-pulse excitation. Such arguments make the outlook for perovskite-based cw lasers very promising, provided that a great effort should be made in terms of reduction of ASE threshold, Auger recombination and thermal resistance.

## 11. Conclusions

This chapter has reviewed the most recent progresses concerning the investigation of the photophysical properties in organolead trihalide perovskites. The absorption spectrum in MAPbI<sub>3</sub> perovskites shows the influence of excitonic states at the band-edge, even if there is evidence that the majority of photogenerated carriers results in free electrons and holes, in a wide excitation range at room temperature. Based on a large body of optical absorption data, the exciton binding energy is estimated to be 23±4 meV by applying the Elliot's theory of Wannier excitons to published absorption spectra; the estimated value stays constant from cryogenic to room temperature. This value is in contrast with what evidenced by magneto-

metry measurements, which provide temperature-dependent values of the exciton binding energy. Additional investigations should be addressed to understand the origin of the discrepancy between what observed by optical spectroscopy and magnetometry.

Trap density in perovskites is significant, like in most solution-processed semiconductors, and its effects emerge particularly under continuous excitation. Although trapping has a negative impact in optoelectronic devices, its capture cross-section happens to be low, as attested by the typical PL lifetime in perovskites exceeding several nanoseconds. The resulting values of carrier mobility can exceed  $10 \text{ cm}^2 \text{ V}^{-1} \text{ s}^{-1}$  and justify the efficient charge collection reported for perovskite-based PV devices.

Emission properties can also play an essential role in the development of new devices based on hybrid perovskites. Many reports provide evidence of amplified spontaneous emission from perovskite thin films under short-pulse excitation, with ASE threshold densities comparable to those of the best state-of-art organic crystals. Under cw pumping, warming suppresses light amplification, in the same way it happens in nitride semiconductors. Similarities between these latter and hybrid perovskites could suggest a way to improve light emission performances in perovskites, in perspective of the realization of a real perovskite-laser.

## Author details

Michele Cadelano, Michele Saba, Nicola Sestu, Valerio Sarritzu, Daniela Marongiu, Feipeng Chen, Roberto Piras, Francesco Quochi, Andrea Mura and Giovanni Bongiovanni\*

\*Address all correspondence to: giovanni.bongiovanni@dsf.unica.it

Dipartimento di Fisica, Università degli Studi di Cagliari, Monserrato, Italy

## References

- [1] Kojima A, Teshima K, Shirai Y, Miyasaka T. Organometal halide perovskites as visible-light sensitizers for photovoltaic cells. *J Am Chem Soc* 2009;131(17):6050.
- [2] Im J, Lee C, Lee J, Park S, Park N. 6.5% efficient perovskite quantum-dot-sensitized solar cell. *Nanoscale* 2011;3(10):4088.
- [3] Kim HS, Lee CR, Im JH, Lee KB, Moehl T, Marchioro A, Moon SJ, Humphry-Baker R, Yum JH, Moser JE, Grätzel M, Park NG. Lead iodide perovskite sensitized all-solid-state submicron thin film mesoscopic solar cell with efficiency exceeding 9%. *Sci Rep* 2012;2:591.
- [4] Burschka J, Pellet N, Moon S, Humphry-Baker R, Gao P, Nazeeruddin MK, Grätzel M. Sequential deposition as a route to high-performance perovskite-sensitized solar cells. *Nature* 2013;499(7458):316.

- [5] Stranks SD, Eperon GE, Grancini G, Menelaou C, Alcocer MJP, Leijtens T, Herz LM, Petrozza A, Snaith HJ. Electron-hole diffusion lengths exceeding 1 micrometer in an organometal trihalide perovskite absorber. *Science* 2013;342(6156):341.
- [6] Xing G, Mathews N, Sun S, Lim SS, Lam YM, Grätzel M, Mhaisalkar S, Sum TC. Long-range balanced electron- and hole-transport lengths in organic-inorganic  $\text{CH}_3\text{NH}_3\text{PbI}_3$ . *Science* 2013;342(6156):344.
- [7] Snaith HJ. Perovskites: the emergence of a new era for low-cost, high-efficiency solar cells. *J PhysChem Lett* 2013;4(21):3623.
- [8] Malinkiewicz O, Yella A, Lee YH, Espallargas GM, Graetzel M, Nazeeruddin MK, Bolink HJ. Perovskite solar cells employing organic charge-transport layers. *Nat Photonics* 2013;8(2):128.
- [9] Park N. Organometal perovskite light absorbers toward a 20% efficiency low-cost solid-state mesoscopic solar cell. *J PhysChem Lett* 2013;4(15):2423.
- [10] Noh JH, Im SH, Heo JH, Mandal TN, Seok Il S. Chemical management for colorful, efficient, and stable inorganic-organic hybrid nanostructured solar cells. *Nano Lett* 2013;13(4):1764.
- [11] Docampo P, Ball JM, Darwich M, Eperon GE, Snaith HJ. Efficient organometal trihalide perovskite planar-heterojunction solar cells on flexible polymer substrates. *Nat Commun* 2013;4:2761.
- [12] Gao P, Grätzel M, Nazeeruddin MK. Organohalide lead perovskites for photovoltaic applications. *Energy Environ Sci* 2014;7(8):2448.
- [13] Ogomi Y, Morita A, Tsukamoto S, Saitho T, Fujikawa N, Shen Q, Toyoda T, Yoshino K, Pandey SS, Ma T, Hayase S.  $\text{CH}_3\text{NH}_3\text{Sn}_x\text{Pb}_{(1-x)}\text{I}_3$  perovskite solar cells covering up to 1060 nm. *J PhysChem Lett* 2014;5(6):1004.
- [14] Eperon GE, Stranks SD, Menelaou C, Johnston MB, Herz LM, Snaith HJ. Formamidinium lead trihalide: a broadly tunable perovskite for efficient planar heterojunction solar cells. *Energy Environ Sci* 2014;7(3):982.
- [15] Noel NK, Stranks SD, Abate A, Wehrenfennig C, Guarnera S, Haghighirad A, Sadhanala A, Eperon GE, Pathak SK, Johnston MB, Petrozza A, Herz LM, Snaith HJ. Lead-free organic-inorganic tin halide perovskites for photovoltaic applications. *Energy Environ Sci* 2014;7(9):3061.
- [16] Lee MM, Teuscher J, Miyasaka T, Murakami TN, Snaith HJ. Efficient hybrid solar cells based on meso-superstructured organometal halide perovskites. *Science* 2012;338(6107):643.
- [17] Deschler F, Price M, Pathak S, Klintberg LE, Jarausch D, Högler R, Huettner S, Leijtens T, Stranks SD, Snaith HJ, Atatuore M, Phillips RT, Friend RH. High photolumi-

- nescence efficiency and optically pumped lasing in solution-processed mixed halide perovskite semiconductors. *J PhysChem Lett* 2014;5(8):1421.
- [18] Xing G, Mathews N, Lim SS, Yantara N, Liu X, Sabba D, Grätzel M, Mhaisalkar S, Sum TC. Low-temperature solution-processed wide wavelength tunable perovskites for lasing. *Nat Mater*. 2014;13(5):476.
- [19] Cadelano M, Sarritzu V, Sestu N, Marongiu D, Chen F, Piras R, Corpino R, Carbonaro CM, Quochi F, Saba M, Mura A, Bongiovanni G. Can trihalide lead perovskites support continuous wave lasing? *Adv Optic Mater* 2015. DOI: 10.1002/adom.201500229.
- [20] Wehrenfennig C, Eperon GE, Johnston MB, Snaith HJ, Herz LM. High charge carrier mobilities and lifetimes in organolead trihalide perovskites. *Adv Mater* 2013;26(10):1584.
- [21] Marchioro A, Teuscher J, Friedrich D, Kunst M, van de Krol R, Moehl T, Grätzel M, Moser JE. Unravelling the mechanism of photoinduced charge transfer processes in lead iodide perovskite solar cells. *Nat Photonics* 2014;8(3):250.
- [22] D'Innocenzo V, Grancini G, Alcocer MJP, Kandada ARS, Stranks SD, Lee MM, Lanzani G, Snaith HJ, Petrozza A. Excitons versus free charges in organo-lead tri-halide perovskites. *Nat Commun* 2014;5:3586.
- [23] Roiati V, Colella S, Lerario G, De Marco L, Rizzo A, Listorti A, Gigli G. Investigating charge dynamics in halide perovskite-sensitized mesostructured solar cells. *Energy Environ Sci* 2014;7(6):1889.
- [24] De Wolf S, Holovsky J, Moon S, Löper P, Niesen B, Ledinsky M, Haug FJ, Yum JH, Ballif C. Organometallic halide perovskites: sharp optical absorption edge and its relation to photovoltaic performance. *J PhysChem Lett* 2014;5(6):1035.
- [25] Zhao Y, Nardes AM, Zhu K. Solid-State Mesostructured perovskite  $\text{CH}_3\text{NH}_3\text{PbI}_3$  solar cells: charge transport, recombination, and diffusion length. *J PhysChem Lett* 2014;5(3):490.
- [26] Giorgi G, Fujisawa J, Segawa H, Yamashita K. Small photocarrier effective masses featuring ambipolar transport in methylammonium lead iodide perovskite: a density functional analysis. *J PhysChem Lett* 2013;4(24):4213.
- [27] Filippetti A, Mattoni A. Hybrid perovskites for photovoltaics: insights from first principles. *Phys Rev B* 2014;89(12).
- [28] Mosconi E, Amat A, Nazeeruddin MK, Grätzel M, De Angelis F. First-principles modeling of mixed halide organometal perovskites for photovoltaic applications. *J PhysChem C* 2013;117(27):13902.

- [29] Kim J, Ho PKH, Murphy CE, Friend RH. Phase separation in polyfluorene-based conjugated polymer blends: lateral and vertical analysis of blend spin-cast thin films. *Macromolecules* 2004;37(8):2861.
- [30] Saba M, Cadelano M, Marongiu D, Chen F, Sarritzu V, Sestu N, Figus C, Aresti M, Piras R, Lehmann AG, Cannas C, Musinu A, Quochi F, Mura A, Bongiovanni G. Correlated electron-hole plasma in organometal perovskites. *NatCommun* 2014;5:5049.
- [31] Hirasawa M, Ishihara T, Goto T, Uchida K, Miura N. Magnetoabsorption of the lowest exciton in perovskite-type compound (CH<sub>3</sub>NH<sub>3</sub>)PbI<sub>3</sub>. *Physica B* 1994;201:427.
- [32] Tanaka K, Takahashi T, Ban T, Kondo T, Uchida K, Miura N. Comparative study on the excitons in lead-halide-based perovskite-type crystals CH<sub>3</sub>NH<sub>3</sub>PbBr<sub>3</sub> CH<sub>3</sub>NH<sub>3</sub>PbI<sub>3</sub>. *Solid State Commun* 2003;127(9-10):619.
- [33] Even J, Pedesseau L, Katan C. Analysis of multivalley and multibandgapabsorption and enhancement of free carriers related to exciton screening in hybrid perovskites. *J PhysChem C* 2014;118(22):11566.
- [34] Yamada Y, Nakamura T, Endo M, Wakamiya A, Kanemitsu Y. Photoelectronicresponses in solution-processed perovskite CH<sub>3</sub>NH<sub>3</sub>PbI<sub>3</sub>solar cells studied by photoluminescence and photoabsorptionspectroscopy. *IEEE J Photovoltaics* 2015;5(1):401.
- [35] Lin Q, Armin A, Nagiri RCR, Burn PL, Meredith P. Electro-optics of perovskite solar cells. *Nat Photonics* 2014;9(2):106.
- [36] Sun S, Salim T, Mathews N, Duchamp M, Boothroyd C, Xing G, Sum TC, Lam YM. The origin of high efficiency in low-temperature solution-processable bilayer organometal halide hybrid solar cells. *Energy Environ Sci* 2014;7(1):399.
- [37] Sestu N, Cadelano M, Sarritzu V, Chen F, Marongiu D, Piras R, Mainas M, Quochi F, Saba M, Mura A, Bongiovanni G. Absorption F-Sum Rule for the Exciton Binding Energy in Methylammonium Lead Halide Perovskites. *J PhysChem Lett* 2015;6:4566.
- [38] Eames C, Frost JM, Barnes PRF, O'Regan BC, Walsh A, Islam MS. Ionic transport in hybrid lead iodide perovskite solar cells. *Nat Commun* 2015;6(7497).
- [39] Zhu H, Fu Y, Meng F, Wu X, Gong Z, Ding Q, Gustafsson MV, Trinh MT, Jin S, Zhy XY. Lead halide perovskite nanowire lasers with low lasing thresholds and high quality factors. *Nat Mater* 2015;14(6):636.
- [40] Tian J, Gao R, Zhang Q, Zhang S, Li Y, Lan J, Qu X, Cao G. Enhanced performance of CdS/CdSe quantum dot cosensitizedsolar cells via homogeneous distribution of quantum dots in TiO<sub>2</sub>film. *J PhysChem C* 2012;116(35):18655.
- [41] Dhanker R, Brigeman AN, Larsen AV, Stewart RJ, Asbury JB, Giebink NC. Random lasing in organo-lead halide perovskite microcrystal networks. *ApplPhys Lett* 2014;105(15):151112.
- [42] Elliot RJ. Intensity of Optical Absorption by Excitons. *Phys Rev* 1957;108(6):1384.

- [43] Sturge MD. Optical absorption of gallium arsenide between 0.6 and 2.75 eV. *Phys Rev* 1963;129(2835).
- [44] Sell DD, Lawaetz P. New analysis of direct exciton transitions: application to GaP. *Phys Rev Lett* 1971;26(6):331.
- [45] Sutherland BR, Hoogland S, Adachi MM, Wong CTO, Sargent EH. Conformal organohalideperovskites enable lasing on spherical resonators. *ACS Nano* 2014;8(10):10947.
- [46] Shah J. *Ultrafast Spectroscopy of Semiconductors and Semiconductor Nanostructures*. Springer; 1999.
- [47] Lanzani G. *The Photophysics behind Photovoltaics and Photonics*. Wiley; 2012.
- [48] Miyata A, Mitoglu A, Plochocka P, Portugall O, Wang JT, Stranks SD, Snaith HJ, Nicholas RJ. Direct measurement of the exciton binding energy and effective masses for charge carriers in organic-inorganic tri-halide perovskites. *Nat Phys* 2015;11(7):582.
- [49] Kitazawa N, Watanabe Y, Nakamura Y. Optical properties of  $\text{CH}_3\text{NH}_3\text{PbX}_3$  (X= halogen) and their mixed-halide crystals. *J Mater Sci* 2002;37(17):3585.
- [50] Buin A, Pietsch P, Xu J, Voznyy O, Ip AH, Comin R, Sargent EH. Materials processing routes to trap-free halide perovskites. *Nano Lett* 2014;14(11):6281.
- [51] Yu H, Wang F, Xie F, Li W, Chen J, Zhao N. The role of chlorine in the formation process of « $\text{CH}_3\text{NH}_3\text{PbI}_{3-x}\text{Cl}_x$ » perovskite. *AdvFunct Mater* 2014;24:7102.
- [52] Bongiovanni G, Staehli JL. Density dependence of electron-hole plasma lifetime in semiconductor quantum wells. *Phys Rev B* 1992;46(15):9861.
- [53] Manser JS, Kamat PV. Band filling with free charge carriers in organometal halide perovskites. *Nat Photonics* 2014;8(9):737.
- [54] Kubo R. Statistical-mechanical theory of irreversible processes. I. *J PhysSocJpn*. 1957;12(6):570.
- [55] Martin PC, Schwinger J. Theory of Many-Particle Systems. I. *Phys Rev* 1959;115(6):1342.
- [56] Smart G. New clues to LEDs' efficiency droop. *Phys Today* 2013;66(7):12.
- [57] Kioupakis E, Rinke P, Delaney KT, Van de Walle CG. Indirect auger recombination as a cause of efficiency droop in nitride light-emitting diodes. *ApplPhys Lett* 2011;98(16):161107.
- [58] Xing J, Liu XF, Zhang Q, Ha ST, Yuan YW, Shen C, Sum TC, Xiong Q. Vaporphase synthesis of organometal halide perovskite nanowires for tunableroom-temperature nanolasers. *Nano Lett* 2015;15(7):4571.

- [59] Leo K, Ruhle W, Ploog KH. Hot-carrier energy-loss rates in GaAs/Al<sub>x</sub>Ga<sub>1-x</sub>As quantum wells. *Phys Rev B* 1988;38(3):1947.
- [60] Pisoni A, Jaćimović J, Barišić OS, Spina M, Gaál R, Forró L, Horvath E. Ultra-low thermal conductivity in organic-inorganic hybrid perovskite CH<sub>3</sub>NH<sub>3</sub>PbI<sub>3</sub>. *J Phys-Chem Lett* 2014;5(14):2488.
- [61] Nakamura S, Senoh M, Nagahama S, Iwasa N, Yamada T, Matsushita T, Kiyoku H, Sugimoto Y, Kozaki T, Umemoto H, Sano M, Chocho K. Continuous-wave operation of InGa<sub>N</sub>/Ga<sub>N</sub>/AlGa<sub>N</sub>-based laser diodes grown on GaN substrates. *ApplPhys Lett* 1998;72(16):2014.

